Response of MCS Low-Frequency Gravity Waves to Vertical Wind Shear and Nocturnal Thermodynamic Environments

FAITH P. GROFF,[a] REBECCA D. ADAMS-SELIN,[b] AND RUSS S. SCHUMACHER[a]

[a] *Department of Atmospheric Science, Colorado State University, Fort Collins, Colorado*
[b] *Atmospheric and Environmental Research, Inc., Lexington, Massachusetts*

(Manuscript received 7 July 2020, in final form 2 September 2021)

ABSTRACT: This study investigates the sensitivities of mesoscale convective system (MCS) low-frequency gravity waves to changes in the vertical wind and thermodynamic profile through idealized cloud model simulations, highlighting how internal MCS processes impact low-frequency gravity wave generation, propagation, and environmental influence. Spectral analysis is performed on the rates of latent heat release, updraft velocity, and deep-tropospheric descent ahead of the convection as a signal for vertical wavenumber $n = 1$ wave passage. Results show that perturbations in midlevel descent up to 100 km ahead of the MCS occur at the same frequency as $n = 1$ gravity wave generation prompted by fluctuations in latent heat release due to the cellular variations of the MCS updrafts. Within a nocturnal environment, the frequency of the cellularity of the updrafts increases, subsequently increasing the frequency of $n = 1$ wave generation. In an environment with low-level unidirectional shear, results indicate that $n = 2$ wave generation mechanisms and environmental influence are similar among the simulated daytime and nocturnal MCSs. When deep vertical wind shear is incorporated, many of the low-frequency waves are strong enough to support cloud development ahead of the MCS as well as sustain and support convection.

KEYWORDS: Gravity waves; Mesoscale systems; Mesoscale models

1. Introduction

Mesoscale convective systems (MCSs) are responsible for the vast majority of precipitation that falls over the plains during the summer months (Fritsch et al. 1986), and they can often be accompanied by flash flooding (Schumacher and Johnson 2005) as well as damaging winds and hail (Fritsch and Forbes 2001). This makes increased predictability highly valuable for forecasters in supporting public safety but also the agricultural, transportation, and insurance industries alike. These factors help demonstrate a few reasons why MCSs are an important and ever-evolving area of study in which the application of findings to numerical weather prediction can help to improve forecasts and the understanding of these intricate systems. Further advancement of this goal, however, requires continued exploration of MCS initiation and sustainment mechanisms, including how low-frequency gravity waves generated by these systems may aid in these processes.

As MCSs develop, the latent heat release throughout the depth of the troposphere causes a gradient between the buoyancy within the convective system and the surrounding stratified environment. In response, nearly hydrostatic and quasi-linear low-frequency gravity waves act to neutralize this imbalance (Schmidt and Cotton 1990; Houze 2004; Fovell et al. 2006; Adams-Selin and Johnson 2013). These waves are defined by the number of antinodes within the vertical latent heating profile during the time of generation. The profile for a convective region, as shown in the top-right panel of Fig. 1a, has a single antinode due to net heating through the depth of the troposphere and would thus classify as an $n = 1$ wave (e.g., Gallus and Johnson 1991; Nicholls et al. 1991; Houze 2004). The profile for the stratiform region, shown in the bottom-right panel of the same figure, has an antinode for the maximum in cooling in the lower levels and another for the maximum in heating in the upper levels, giving an $n = 2$ wave. The speed at which these low-frequency gravity waves travel is

$$c = \frac{NH}{n\pi}, \tag{1}$$

c being the gravity wave speed (m s^{-1}), N the Brunt–Väisälä frequency (s^{-1}), H the height of the tropopause (m), and n the number of the gravity wave of interest (Nicholls et al. 1991).

Nicholls et al. (1991) found that the convective heating profile induced deep-tropospheric descent and adiabatic warming at the $n = 1$ gravity wave front, subsequently stabilizing the environment and suppressing new convection as the wave propagated away from the system (Fig. 1a). The stratiform heating profile, conversely, produced an $n = 2$ wave that prompted ascent through the bottom half of the troposphere and descent in the upper half, supporting adiabatic cooling and warming, respectively, as shown in Fig. 1b. The low-level adiabatic cooling introduced by this wave was found to have a critical influence in destabilizing the environment by increasing the convective available potential energy (CAPE) and decreasing the convective inhibition (CIN; Mapes 1993; McAnelly et al. 1997). Numerical simulations and cloud-resolving models agree with the results obtained from these analytical solutions: $n = 1$ waves suppress new convection by increasing stability (e.g., Lane and

Groff's current affiliation: CPP Wind Engineering and Air Quality Consultants, Windsor, Colorado.

Corresponding author: Faith P. Groff, Fgroff@cppwind.com

DOI: 10.1175/JAS-D-20-0208.1

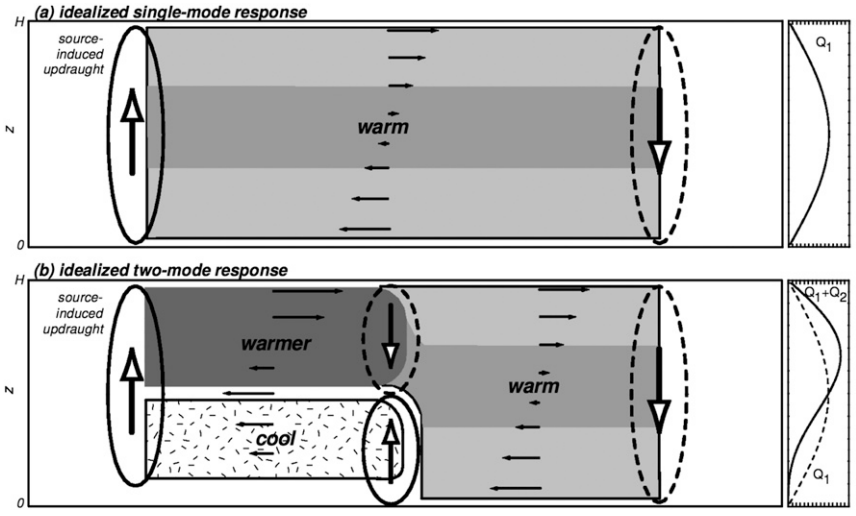

FIG. 1. Downstream response to sustained vertical heating profiles that generate (a) an $n = 1$ wave and (b) an $n = 2$ wave. Figures 11a and 11b from Fovell (2002), adapted from Nicholls et al. (1991) and Mapes (1993).

Reeder 2001; Fovell 2002; Fovell et al. 2006; Adams-Selin 2020a), and $n = 2$ waves decrease stability through adiabatic cooling (e.g., Fovell et al. 2006; Lane and Zhang 2011; Adams-Selin and Johnson 2013; Adams-Selin 2020a).

Fovell (2002) and Fovell et al. (2006) noted how the adiabatic cooling introduced by $n = 2$ waves can create a low-level, nearly saturated layer with decreased static stability in which high-frequency waves can serve as a catalyst for convection initiation (CI). This moist layer and additional $n = 2$ wave processes can also help to sustain or even strengthen an MCS. Building upon the broad statements of MCS reinvigoration by $n = 2$ waves in Mapes (1993) and McAnelly et al. (1997), Adams-Selin and Johnson (2013) showed that the increased CAPE within the subsaturated layer can become part of the inflow to the MCS and strengthen the convective updrafts. This positive feedback mechanism between environments influenced by $n = 2$ wave passage and the intensification of the parent system is also seen in single convective clouds in Lane and Zhang (2011) as well as supercells in Trapp and Woznicki (2017).

Recent studies have begun to explore the generation of multiple low-frequency gravity waves from one convective system. Adams-Selin and Johnson (2013) observed multiple $n = 1$ waves within observations as well as a cloud model simulation of the same event, attributing each wave to changes within the vertical heating profile. Adams-Selin (2020a) built upon this theory by connecting changes in the heating profile and subsequent gravity wave generation to periodic reintensifications of the updraft. These studies suggest that $n = 1$ gravity wave generation can be linked to the characteristic cellularity of MCSs, a process also noted of convective cloud fields in Lane and Zhang (2011).

Can $n = 1$ gravity wave generation be definitively associated with the cellularity of MCS updrafts? How do low-frequency gravity waves modify the environment, and are these modifications enough to make conditions more or less favorable for cloud development and CI? Through the incorporation of nonlinear influences by Cloud Model 1 (CM1) simulations, this study will address these questions as well as their sensitivities to deep vertical wind shear and nocturnal environments to further advance our understanding of the connections between MCSs and low-frequency gravity waves.

The methodology and CM1 model configuration are detailed in section 2. Section 3 sets the foundation for this work through the analysis of a highly idealized MCS. Low-frequency gravity wave sensitivities to varying vertical wind and thermodynamic profiles are explored in section 4. Finally, the conclusions from this work will be discussed in section 5.

2. Model configuration and initialization

In this study, CM1 version 18.3 is used with a configuration similar to that used in Adams-Selin (2020a). The domain extends 350 km × 300 km with 250-m horizontal grid spacing, while the uniform vertical grid spacing is 100 m through 16 km. The "cold pool–dam break" (Weisman et al. 1997) mechanism is used to initiate convection, and the Morrison microphysical parameterization with hail as the dense rimed ice class (Morrison et al. 2009) is applied. The Morrison scheme has been studied extensively for MCSs (e.g., Bryan and Morrison 2012) and predicts two moments for rain, graupel, cloud water, and cloud ice, which are important quantities for evaluating latent heating profiles that are not available in the other candidate parameterizations.

The initial conditions for the Control simulation are defined by the Weisman and Klemp (1982) thermodynamic profile, modified to increase the mixing ratio from the surface to the LCL to 16.2 g kg^{-1} as in Adams-Selin (2020a), paired with a linear vertical wind shear profile of 5 m s^{-1} easterly winds at the surface tapering to 0 m s^{-1} by 5 km. The Brunt–Väisälä frequency, N, was smoothed to remove unforeseen trapping

TABLE 1. Configuration of CM1 experiments.

Simulation	Thermodynamic profile	Wind profile
Control	Weisman–Klemp	5 m s^{-1} linear shear
Wind	Weisman–Klemp	PECAN observed
Thermo	PECAN observed, with low-level moisture adjustment	5 m s^{-1} linear shear
Nocturnal	PECAN observed, with low-level moisture adjustment	PECAN observed

layers, and the potential temperature was adjusted accordingly assuming no changes to water vapor content. This was done in order to place focus on the low-frequency waves generated from the convection itself, and considering that the Scorer parameter reveals that there are no trapping levels present in the environment, this excludes the potential for any elevated bore processes such as those in Zhang et al. (2020).

The next three simulations each incorporate aspects of a sounding collected during the Plains Elevated Convection at Night (PECAN) field campaign (Geerts et al. 2017). On the night of 14/15 July 2015, the campaign embarked on a CI mission in eastern Colorado. The convection quickly organized into an MCS that marched through Kansas with the leading convective line extending through Nebraska and a rapidly developing stratiform region trailing behind. As the storm began to bow and the stratiform region widened, multiple radar fine lines propagated away from the MCS. Grasmick et al. (2018) found that on the southern portion of the storm, both density currents and bores could be identified; however, the wind profile on the northern edge of the system was not favorable for such processes. The unclassified fine line produced from this portion of the MCS serves as the inspiration for using the Hays, Kansas, proximity sounding taken at 0523 UTC 15 July 2015, just before the MCS passed through the area and prior to the passage of the radar fine line, in these simulations.

The wind profile of the PECAN sounding is smoothed using the 1–2–1 method, and for the simulations that incorporate this shear profile, a 5.4 m s^{-1} northerly wind is added to the initialization profile to contain the leading line of convection within the domain. The thermodynamic profile is modified to include an

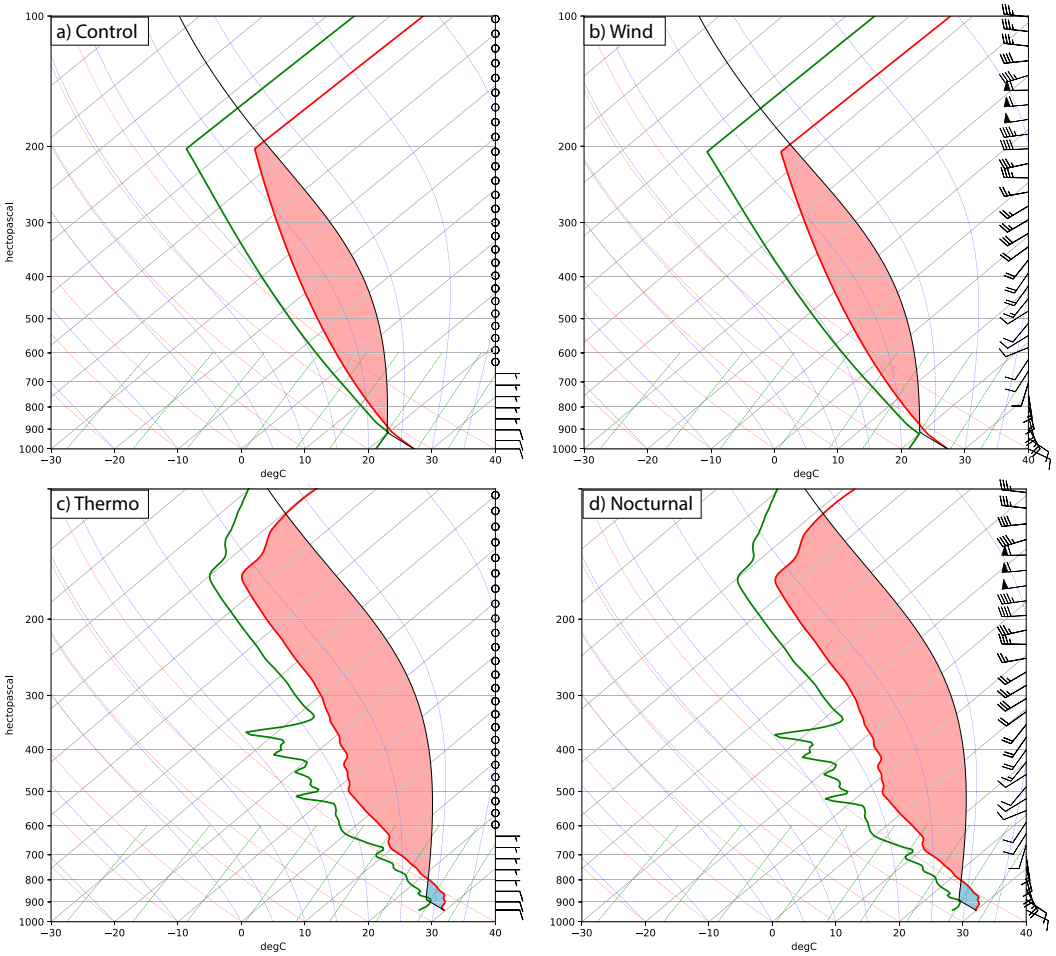

FIG. 2. Skew T–log$p$ diagrams of the soundings used to initialize the (a) Control, (b) Wind, (c) Thermo, and (d) Nocturnal simulations. The black lines delineate the parcel path, and the red and blue shaded regions indicate CAPE and CIN, respectively, in J kg^{-1}.

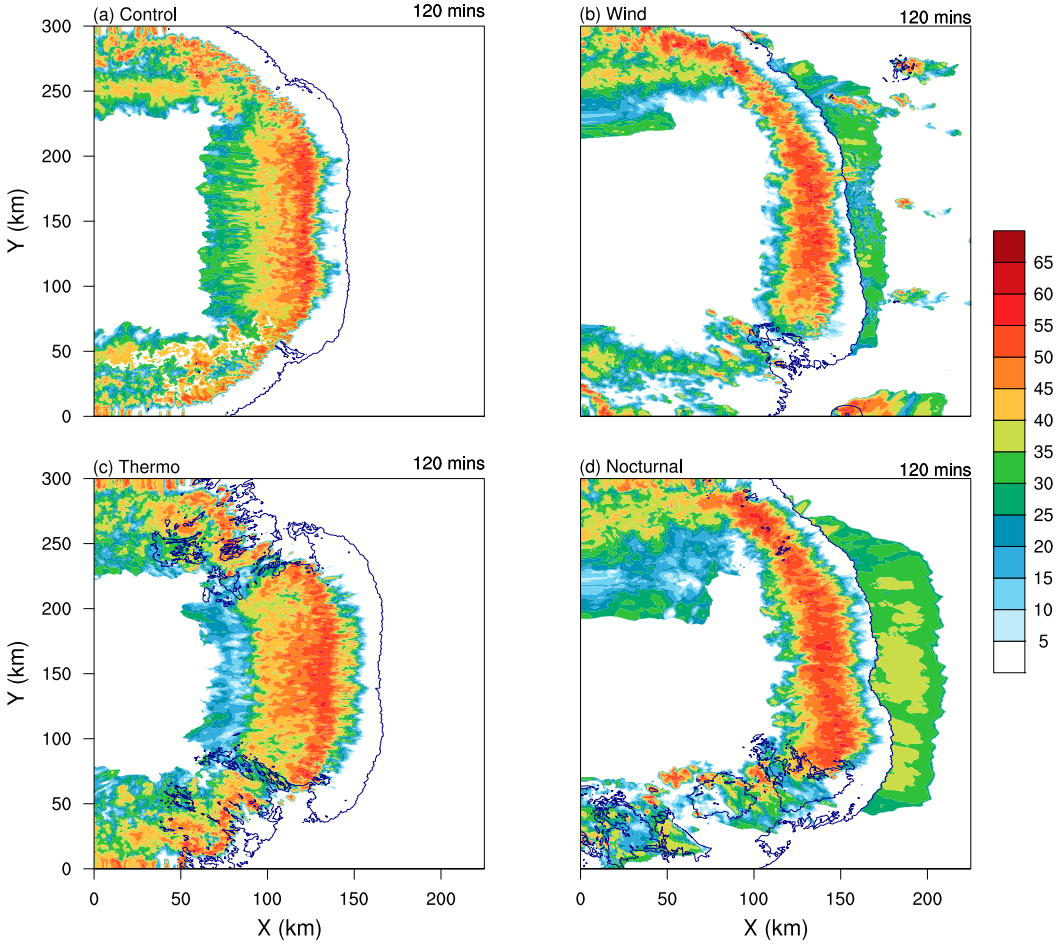

FIG. 3. Surface reflectivity at $t = 120$ min for the mature MCSs within the (a) Control, (b) Wind, (c) Thermo, and (d) Nocturnal simulations with their respective cold pools, defined as the −2-K potential temperature perturbation, indicated by the navy contours.

increase in relative humidity by 20% in the lowest 200 hPa, the amount of additional moisture needed to produce an MCS similar to the one observed. Increasing the moisture of the initialization environment in order to simulate realistic convection is a common practice (e.g., Peters and Schumacher 2016), and this is particularly true for environments with CIN (e.g., Parker and Johnson 2004; Naylor and Gilmore 2012), as in this sounding. Although the additional moisture increases the most unstable CAPE (MUCAPE) from 5320 to 8164 J kg^{-1}, a value significantly greater than any sampled during the PECAN field campaign (Hitchcock et al. 2019), the MCSs initialized using this thermodynamic profile still share a similar intensity to the observed MCS as detailed in section 4c. The temperature and relative humidity profiles are also smoothed by the 1–2–1 method, and the stratospheric variables were extrapolated from approximately 14 to 16 km.

To understand the sensitivity of low-frequency gravity waves to vertical wind shear more common of midlatitude MCSs, the second CM1 simulation of this study, hereafter called Wind, uses the Control thermodynamic profile and the smoothed PECAN vertical wind profile for the initial conditions. The Thermo experiment isolates how a nocturnal thermodynamic environment may modify gravity wave generation and influence independent of the wind profile. The initial sounding for this experiment uses the Control wind shear profile and the PECAN thermodynamic profile. Finally, the Nocturnal simulation employs the full modified PECAN sounding to mimic a nocturnal MCS that includes a low-level jet (LLJ) as well as a stable boundary layer. A summary of each CM1 simulation can be found in Table 1.

3. Analysis of an idealized MCS

A highly idealized MCS is simulated in CM1 to provide a foundation for comparison among the simulations with varying vertical wind and/or thermodynamic profiles. The initial Control sounding is shown in Fig. 2a. This environment produced an organized MCS with an expansive trailing stratiform region (Fig. 3a). Unless otherwise specified, all analysis is conducted for a 5-km averaged domain centered about $y = 125$ km.

The greatest descent associated with an $n = 1$ gravity wave front should occur around the same height as the largest latent

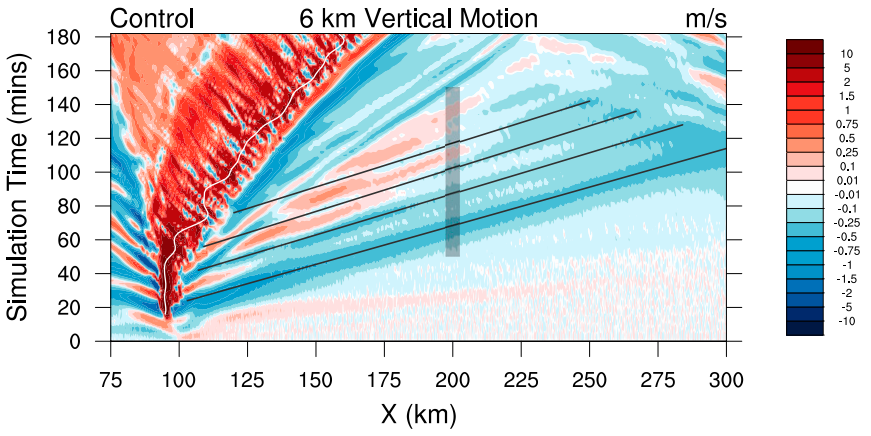

FIG. 4. Hovmöller diagram of vertical motion (m s^{-1}) at 6 km in the Control simulation. Gray lines delineate each $n = 1$ gravity waves' propagation downstream. The white line is the location of the maximum updraft velocity at this height, and the transparent black box centered over $x = 200$ km shows the domain of preconvective descent analyzed in spectral analysis.

heat release within an MCS, generally about half the height of the tropopause (Nicholls et al. 1991). By looking at a Hovmöller diagram of vertical motion at that height, $n = 1$ waves can be tracked as they move through the forward environment. Four such waves are analyzed in this simulation at 6 km and are shown by the gray lines in Fig. 4. The vertical structure of two of these waves can be identified by the regions of deep-tropospheric descent centered around $x = 170$ and 215 km in Fig. 5.

The largest rates of latent cooling within the MCS occur near or below the freezing level, around 3 km in this simulation as seen in Fig. 6, thus any $n = 2$ waves can be followed through the forward environment by identifying areas of enhanced ascent around the same height. By this method, three $n = 2$ waves are identified by the dashed gray lines in Fig. 7. The vertical structure of the first of these $n = 2$ waves can be seen centered around $x = 140$ km in Fig. 5, where ascent is met with descent around half the height of the tropopause. The Hovmöller diagrams can also be used to find the approximate time each wave is generated, and through the application of the time–height diagrams of latent heating and cooling, aid in identifying the processes occurring in the MCS at the time of generation.

a. n = 1 gravity wave generation

The updraft velocity and rate of latent heat release within the system both demonstrate a cyclical nature with life cycles between 15 and 20 min as shown in Figs. 8 and 9, respectively, which implies that there should be a number of $n = 1$ gravity waves generated from this system in response to changes in the vertical latent heating profile (Lane and Zhang 2011; Adams-Selin and Johnson 2013; Adams-Selin 2020a). The first $n = 1$ gravity wave appears approximately 20 min into the simulation as the storm begins to develop and the updraft takes form. Cycling of the updrafts generates more $n = 1$ waves in

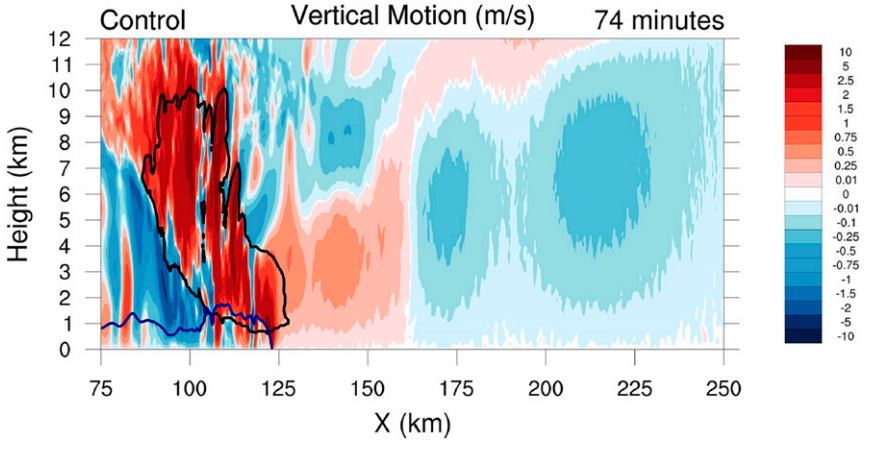

FIG. 5. Vertical cross section of vertical motion (m s^{-1}) at $t = 74$ min in the Control simulation. The blue contour indicates the location of the cold pool, defined as the −2-K potential temperature perturbation, and the black contour the 0.01 g kg^{-1} cloud mixing ratio.

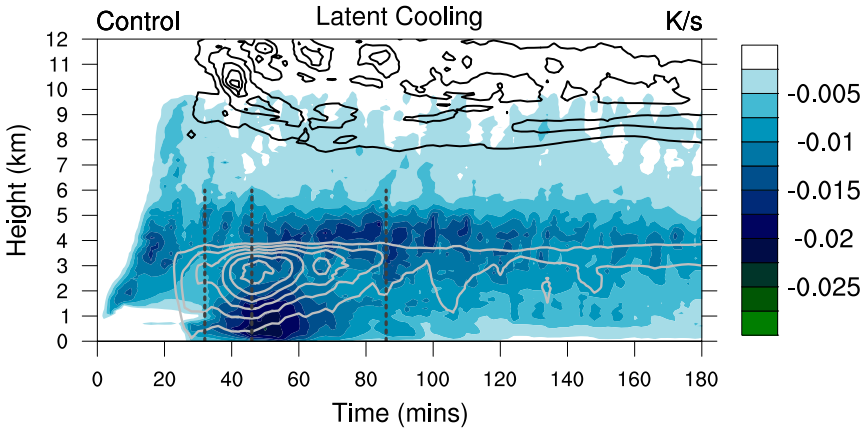

FIG. 6. Time–height diagram of the 95th-percentile values of negative changes to the potential temperature field by microphysical processes (K s^{-1}) for the Control simulation. Shaded colors show rates of evaporational cooling. Latent cooling due to melting is represented by the light gray contours from -0.014 to -0.002 K s^{-1} by 0.002 K s^{-1}, and the black contours show cooling from sublimation from -0.75 to -0.05 K s^{-1} by 0.1 K s^{-1}. Dashed gray lines indicate approximate times of $n = 2$ gravity wave generation as determined from Fig. 7.

response, and these appear after each respective maximum in latent heat release as shown by the vertical gray lines in Fig. 9.

SPECTRAL ANALYSIS

As the storm matures and begins to develop a trailing stratiform region, the gravity waves become increasingly difficult to subjectively discern after extensive environmental modulation by preceding wave activity closer to the convective line. To objectively identify the frequency of $n = 1$ wave initiation and subsequent influence on the forward environment, spectral analysis is performed on three principal variables within this mechanism: updraft velocity and latent heat release as signals for generation, and deep-tropospheric descent as the signal for environmental modulation. A time series of the 95th-percentile values of these variables between 5 and 8 km (Fig. 10) shows that the updraft velocity and latent heat release have a clear cyclical nature and vary concurrently. As low-frequency waves begin to travel across the analysis domain ahead of the convection (represented by the black box in Fig. 4) starting around 60 min, the time series of descent shows periodicity similar to the cyclical nature of the updraft and latent heating time series. For all negative variables within this study, the 95th percentile corresponds to absolute magnitude.

Spectral analysis [see Wilks (2011) for reference] is employed to distinguish sine and cosine wave patterns within these time series to objectively identify at what frequency they each demonstrate cellularity. After removing the series mean and least squares linear trend, each time period of analysis is tapered by 10% to avoid spectral leakage. This statistical method is first applied to the updraft and latent heating time series between 10 and 110 min. To increase the degrees of freedom, the power spectrum is calculated every 250 m for 5 km centered about $y = 125$ km, the otherwise averaged domain.

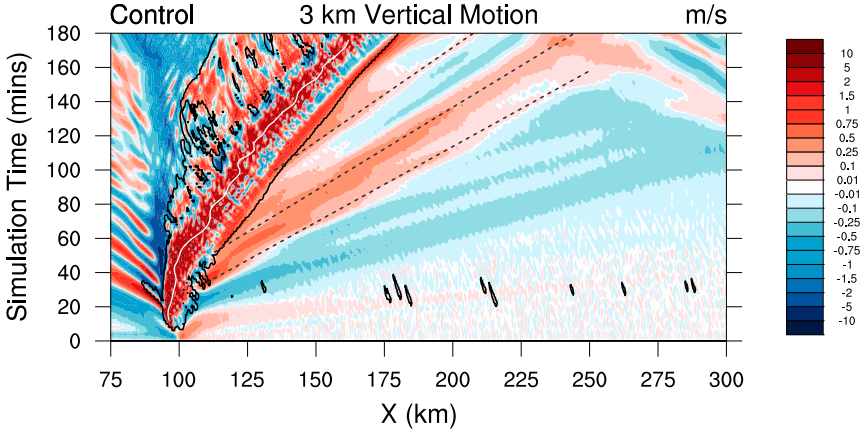

FIG. 7. As in Fig. 4, but at $z = 3$ km. Dashed gray lines show three $n = 2$ waves and their propagation ahead of the convective line.

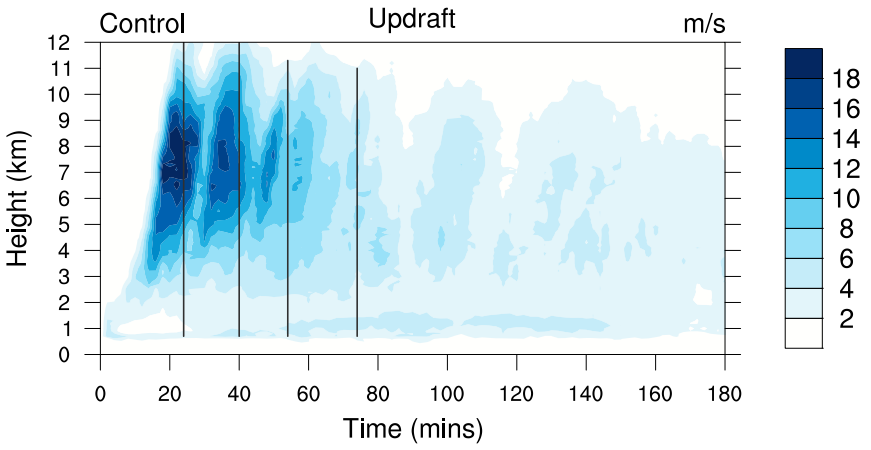

FIG. 8. Time–height diagram of the 95th-percentile values of updraft velocity ($m\ s^{-1}$) in the Control simulation. The gray lines indicate approximate times of $n = 1$ gravity wave generation as determined from Fig. 4.

At this spatial resolution, the power spectrum is then calculated for 21 time series. Numerical models are generally able to resolve independent features approximately every 6–10 Δx (Skamarock 2004); therefore, this study will approximate 6 degrees of freedom for the spectra. The same process was conducted for the preconvective descent time series between 50 and 150 min.

The power spectra for updraft velocity, latent heat release, and preconvective descent (Fig. 11) all show significant peaks at 0.12 cycles $(2\ min)^{-1}$ (the model output frequency), indicating that these three parameters manifest maximums at the same frequency. This strongly suggests that the $n = 1$ waves are generated by alterations in latent heating due to the cyclical variations in the updrafts, and that the same $n = 1$ waves are leading to regular perturbations of midlevel descent up to 100 km ahead of the system. These robust results imply that even as the stratiform region expands and becomes increasingly more influential on the MCS's latent heating profile as discussed in Houze (2004), $n = 1$ waves are likely still being generated through 110 min into the simulation alongside higher-order wave modes even though their influence may become harder to subjectively discern.

b. $n = 2$ gravity wave generation

As the MCS transitions into maturity, the convective updrafts weaken in intensity, the latent heating is reduced, and another mode of low-frequency gravity waves becomes more favorable for generation (Lane and Reeder 2001). Established low-frequency gravity wave theory suggests that $n = 2$ waves are generated in response to increases in cooling within the lower half of the troposphere associated with sublimation, melting, and evaporation of hydrometeors. Variables such as stratiform precipitation and mesoscale downdrafts influence the latent cooling within an MCS, and their dynamics are generally less cyclical and more sporadic in nature. This renders the

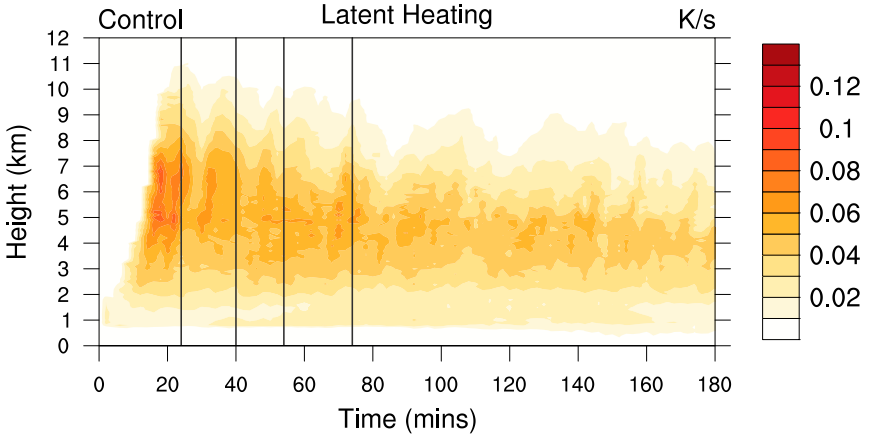

FIG. 9. Time–height diagram of the 95th-percentile values of positive changes to the potential temperature field due to microphysical processes ($K\ s^{-1}$) in the Control simulation. The gray lines indicate approximate times of $n = 1$ gravity wave generation as determined from Fig. 4.

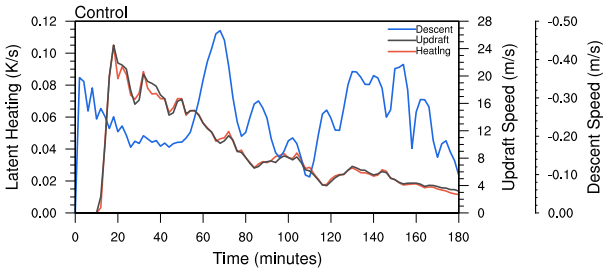

FIG. 10. Time series of the 95th-percentile values of the updraft velocity, microphysical heating, and preconvective descent within the Control simulation, represented by the gray, red, and blue lines, respectively. The area over which the preconvective descent is calculated is shown in Fig. 4.

process and timing behind $n = 2$ gravity wave generation different than those of $n = 1$ gravity waves.

As shown in Fig. 6, the first distinguishable $n = 2$ gravity wave is generated roughly 30 min into the simulation, just as rain and hail begin to descend to the surface. A second $n = 2$ gravity wave is generated approximately 45 min into the simulation as the storm begins to widen and separate into distinct regions of stratiform and convective precipitation, a generation mechanism also noted in Fovell (2002) and Adams-Selin (2020a). This transition prompts the largest latent cooling response of the entire simulation due to the increased rates of melting and evaporation as shown by the second dashed line in Fig. 6. The second $n = 2$ wave generated around this time then also has the strongest low-level ascent, and its environmental impact can be followed by the second dashed line in Fig. 7.

c. *Environmental response*

Each wave mode has a particular area of influence that can suppress or support the stability of the surrounding environment. The first two $n = 1$ waves adiabatically warm the depth of the troposphere through descent, reducing the MUCAPE field by over 100 J kg^{-1} for each wave passage as shown by the solid lines in Fig. 12. The greatest heating occurs where the descent is maximized, in the midlevels, and so the $n = 1$ waves have a particularly strong influence on CAPE. The largest adiabatic cooling contribution occurs at the same level as the greatest $n = 2$ wave prompted ascent, around 3 km in this simulation. This causes the $n = 2$ waves to have less of an influence on CAPE but a greater influence on the LFC. As seen in Fig. 13, the deep-tropospheric descent and adiabatic warming induced by the two $n = 1$ waves causes the LFC to increase by at least 25 m. However, the $n = 2$ waves counteract the influence of the $n = 1$ waves. The first $n = 2$ wave lowers the LFC by 25 m. The second, stronger $n = 2$ wave lowers the LFC even past its original height. These results are consistent with those found in Lane and Reeder (2001), Adams-Selin and Johnson (2013), and Adams-Selin (2020a,b): stability parameters are sensitive to each wave's height of maximum influence.

4. MCS and low-frequency gravity wave sensitivities

The following sections will focus on a series of sensitivity tests in which low-frequency gravity waves are studied within environments that incorporate components of a proximity sounding collected minutes before the passage of an observed MCS. A summary of each CM1 simulation can be found in Table 1.

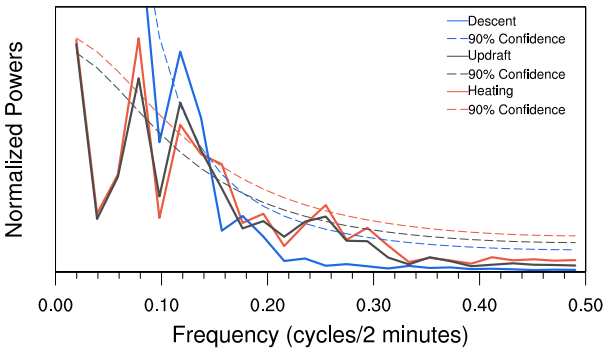

FIG. 11. The power spectrum for updraft velocity (gray), latent heat release rate (red), and preconvective descent (blue) in the Control simulation. Dashed lines represent the 90% confidence intervals for each variable of the same color. Each spectra was normalized so that the area under the line equals the variance of the detrended time series.

a. *Vertical wind shear*

Dissimilarities between the Control run and this simulation are the result of deep shear impacts on the internal dynamics of an MCS. The Control simulation uses an idealized wind profile limited to weak low-level shear while the vertical wind shear profile used in this simulation introduces an LLJ with stronger line-normal shear below moderate westerly shear aloft (Fig. 2b).

There are a few key differences between the internal dynamics and structure of the MCS in this simulation and the Control run that contribute to changes in low-frequency gravity wave generation and strength. One of the most notable features is that the trailing stratiform region for the Wind simulation MCS is much more confined (cf. Figs. 3a,b). This drastically restricts the horizontal extent over which latent cooling occurs, placing the vast majority of cooling within the convective downdrafts compared to the moderate distribution of cooling over the stratiform region of the control MCS. The Wind simulation MCS is also stronger in overall intensity as shown by the higher updraft velocities for this case in Fig. 14. This is to be expected as the incorporation of stronger line-normal shear has been shown to increase the strength of the cells within an MCS compared to environments such as the one in the Control simulation (Rotunno et al. 1988; Markowski and Richardson 2011).

1) $n = 1$ GRAVITY WAVE GENERATION

As with the Control simulation, the driver of $n = 1$ gravity wave generation in this simulation lies within the cellular nature of the updrafts and subsequent latent heat release. The first four $n = 1$ gravity waves appear promptly after each respective maximum in latent heating as seen in Fig. 15a. The four waves have been subjectively analyzed by the deep-tropospheric descent propagating away from the convection as identified in Fig. 16a, but it is obvious from Fig. 15a that the

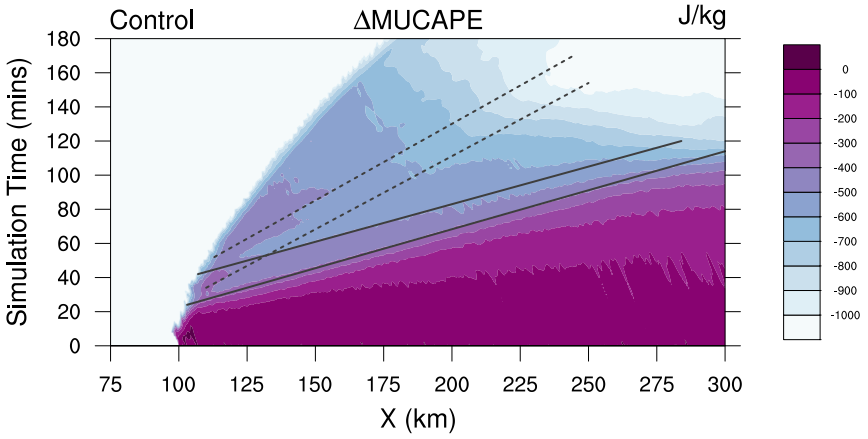

FIG. 12. Hovmöller diagram of the change in MUCAPE from the initial environment (J kg^{-1}) in the Control simulation. The solid lines show the paths of the first two $n = 1$ waves and the dashed lines the first two $n = 2$ waves.

cyclical nature of the latent heat release does not stop after the generation of those four waves.

Spectral analysis is performed on the same three $n = 1$ gravity wave variables as in section 3a(1) to provide additional support for low-frequency gravity wave generation mechanisms and environmental influence but within a deep-shear environment. The analysis is performed over the same y domain cross section, but instead only 2 degrees of freedom are allotted as this method averages together the individual variables over the domain instead of calculating spectra for each point. This method aids in reducing noise and highlighting the true processes occurring within this more chaotic environment.

The resulting spectra are shown in Fig. 17a. As in the Control simulation, the three variables all have matching, significant spectra at 0.12 cycles (2 min)$^{-1}$. In response to this vertical wind profile, the MCS consistently has stronger updrafts and associated higher magnitudes of latent heat release, yet even with this change to the internal dynamics of the system, the updrafts still show the same life cycle period and remain the dominant factor in the generation frequency of these waves. This modified wind profile does not change the generation frequency of $n = 1$ gravity waves, only their strength.

2) $n = 2$ GRAVITY WAVE GENERATION

While the timing of $n = 1$ waves depends largely on the cellularity of the updrafts, the signals for $n = 2$ gravity wave generation are not as clear and can differ greatly among the simulations. In the Control simulation, the onset of precipitation to the surface occurs just before the generation of the first $n = 2$ wave, but the same initial surge of cooling is not enough to prompt the generation of an $n = 2$ wave in this case. The Control simulation's weak mid- and upper-level winds scarcely advect hail away from the convective line, concentrating the majority of latent cooling to this region at the start of the simulation. As melting extends to the surface with the onset of precipitation as seen in Fig. 6, the first $n = 2$ gravity wave of that simulation is generated. For the Wind simulation, stronger updrafts and mid- to upper-level storm-relative winds keep the hail above the melting level, identified around 4 km from Fig. 18a, longer than in the Control run. When precipitation first descends to the

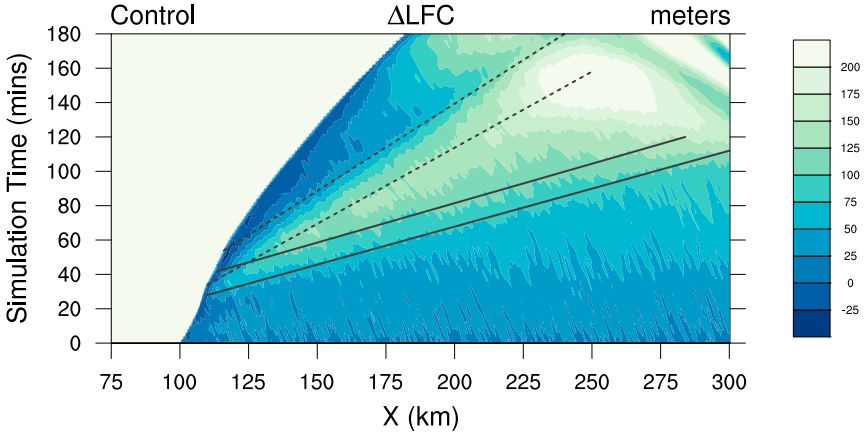

FIG. 13. As in Fig. 12, but for the LFC in meters.

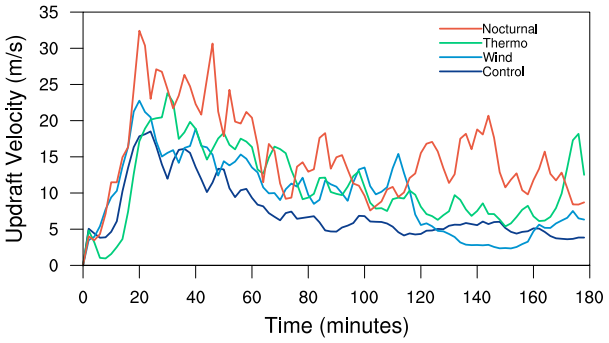

FIG. 14. The 99th-percentile values of vertical motion within the troposphere for the Control (navy), Wind (light blue), Thermo (green), and Nocturnal (red) simulations.

surface around 25 min, there is little cooling contribution from melting in the lower levels. Consequently, the magnitude of latent cooling over the lower levels at this time is not enough to support the generation of an $n = 2$ wave.

When "fingers" of reflectivity, an element examined within idealized models (Bryan et al. 2007) and in many of the MCSs studied in the PECAN field campaign (Geerts et al. 2017), begin to extend from the convective line ahead of the storm around 35 min into the Wind simulation, they are accompanied by a surge of precipitation to the surface that includes hail and introduces additional cooling by melting in the lower levels outside of the downdraft. Quickly following this increase and horizontal expansion of low-level latent cooling, the first $n = 2$ wave of the simulation can be identified through low-level ascent shown by the first dashed line in Fig. 19a.

Just after 60 min into the simulation, a strong downdraft occurs within the MCS as indicated by the surge in latent cooling shown in Fig. 18a. Evaporational cooling below cloud base contributes to the increase in latent cooling, but there is also a large contribution from melting due to the increased amounts of hail caught in the downdraft. The second $n = 2$ wave, indicated by the second dashed line in Fig. 18a, is generated about this time. Around 120 min into the simulation, the updraft weakens considerably (Fig. 14) and is no longer able to suspend larger hydrometeors. Hail fallout can be followed through the storm in Fig. 18a as the values of latent cooling due to melting increase around this time, and shortly thereafter, the rates of evaporative cooling increase rapidly as the hydrometeors descend below cloud base. The large increase in latent cooling to the lower levels in combination with the decrease in latent heating in the mid- to upper levels supports an environment theorized to be more conducive for $n = 2$ wave generation, and the third $n = 2$ wave of the simulation is generated around this time.

3) ENVIRONMENTAL RESPONSE

Overall, the $n = 1$ waves in this simulation are stronger than the same waves in the Control simulation due to the higher rates of latent heat release. The descent at 6 km associated with the first two $n = 1$ waves can be seen throughout the entire domain (Fig. 16a) even after interacting with single cell convection between 200 and 300 km. Consistent with the Control simulation, the passage of each $n = 1$ wave acts to decrease the amount of MUCAPE, but in this simulation that reduction at times approaches 200 J kg^{-1} at points closer to the convective line where the vertical motion associated with the waves is strongest (cf. Figs. 20a and 16a).

The influence of $n = 2$ waves can often be minimized when overrun by $n = 1$ waves that move at twice the speed, but the impacts these waves have are still significant. The passage of each $n = 2$ wave, shown by the dashed lines in Fig. 21, corresponds to a decrease in the LFC by at least 25 m. In this environment, this aids in the development of clouds ahead of the MCS. This influence can be seen with each of the three $n = 2$ waves in Fig. 19a, where the black line contour represents the 0.01 g kg^{-1} cloud mixing ratio and the dashed lines are the three analyzed $n = 2$ waves. The clouds associated with the convection are drawn out with the $n = 2$ waves as they propagate away from the MCS.

This is the only case to develop spurious convection ahead of the MCS. While it is likely a result of model noise, the impacts that gravity waves have on the new convection can still be studied. The single convective cell first appears ahead of the MCS approximately 50 min into the simulation and continues for the duration of the run. As seen in Fig. 22a, 100 min into the simulation, the MCS is strong, well organized, and catching up to the cell approximately 50 km downstream. A dense concentration of hail lofted well into the upper levels shows the strength and vertical extent of the MCS updrafts. The cell downstream has begun to precipitate and even has a small amount of hail within the storm as it progresses into maturity. Just over 20 min later, both the MCS and the single convective cell have weakened significantly as seen in Fig. 22b by the notable decrease in hydrometeors. The last $n = 2$ wave is generated around this time after the rapid evaporation and melting of hydrometeors no longer suspended aloft by the weakened updrafts causes a large latent cooling response (Fig. 18a). This wave decreases the LFC by at least 25–50 m as it propagates away from the MCS as shown by the last dashed line in Fig. 21. When this wave interacts with the remnants of the decayed cell, its accompanied low-level ascent and increased relative humidity quickly revive the cell just before 136 min into the simulation as shown in Fig. 22c. Within minutes, the cell is further strengthened when it interacts with the vertical motion associated with the MCS's cold pool. When the cell is absorbed by the MCS, the accompanied moisture and buoyancy aid in the revival of the system. Immediately following, the updraft velocity and associated latent heat release both show increases in magnitude as seen in Figs. 14 and 15a after 160 min into the simulation. This succession has also been observed in Fovell et al. (2006), Adams-Selin and Johnson (2013), and Adams-Selin (2020a).

The $n = 2$ wave directly assists in the resurgence of the MCS by reviving the single convective cell later absorbed by the MCS, providing much needed buoyancy and moisture to the system. These results are similar to those seen in Fovell et al. (2006); however, the key difference between these mechanisms is that the new cell is not generated by high-frequency waves as in that study but likely by model noise. Regardless, the $n = 2$ wave has a direct impact on the convective cell that affords it additional time for propagation and sustainment, which in turn later provides the same support to the MCS once absorbed. This is an exciting result that not only further supports how cell

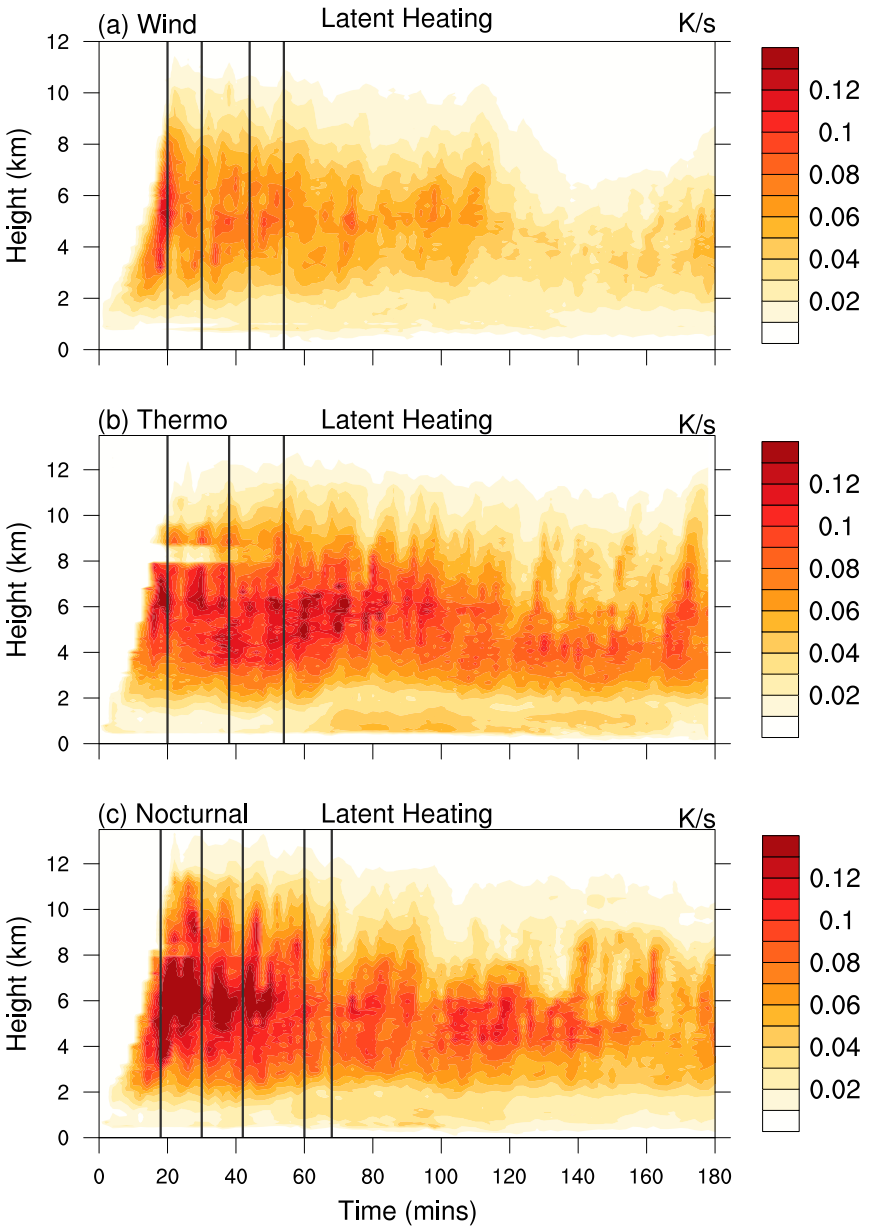

FIG. 15. As in Fig. 9, but for the (a) Wind, (b) Thermo, and (c) Nocturnal simulations and their respective $n = 1$ wave generation times as determined from Fig. 16.

absorption can have a positive influence on the system, but also that $n = 2$ waves are capable of strengthening and reviving cells downstream.

b. *Nocturnal thermodynamic environment*

The environment used to initialize this simulation (Fig. 2c) utilizes the same idealized wind shear profile as the Control simulation; however, the thermodynamic profile is a slightly modified version of the nocturnal PECAN profile detailed in section 2. Though the nocturnal boundary layer is just under 100 hPa deep, the stable layer introduces enough CIN to generally hinder surface parcels, rendering the convection elevated just as the MCS sampled from PECAN. Parcels that are able to reach the LFC (located around 1360 m) have access to a large amount of MUCAPE, emphasizing the important potential influence that $n = 2$ waves can have in this environment. The increase in MUCAPE causes the intensity of this system to exceed that of the Control and Wind simulations, but the limited easterly low-level shear profile inhibits the sustainment of the stronger cells similar to the MCS life cycle in the Control simulation (Fig. 14).

1) $n = 1$ GRAVITY WAVE GENERATION

The MCS produced in this environment has the same general life cycle and structure as the MCS in the Control

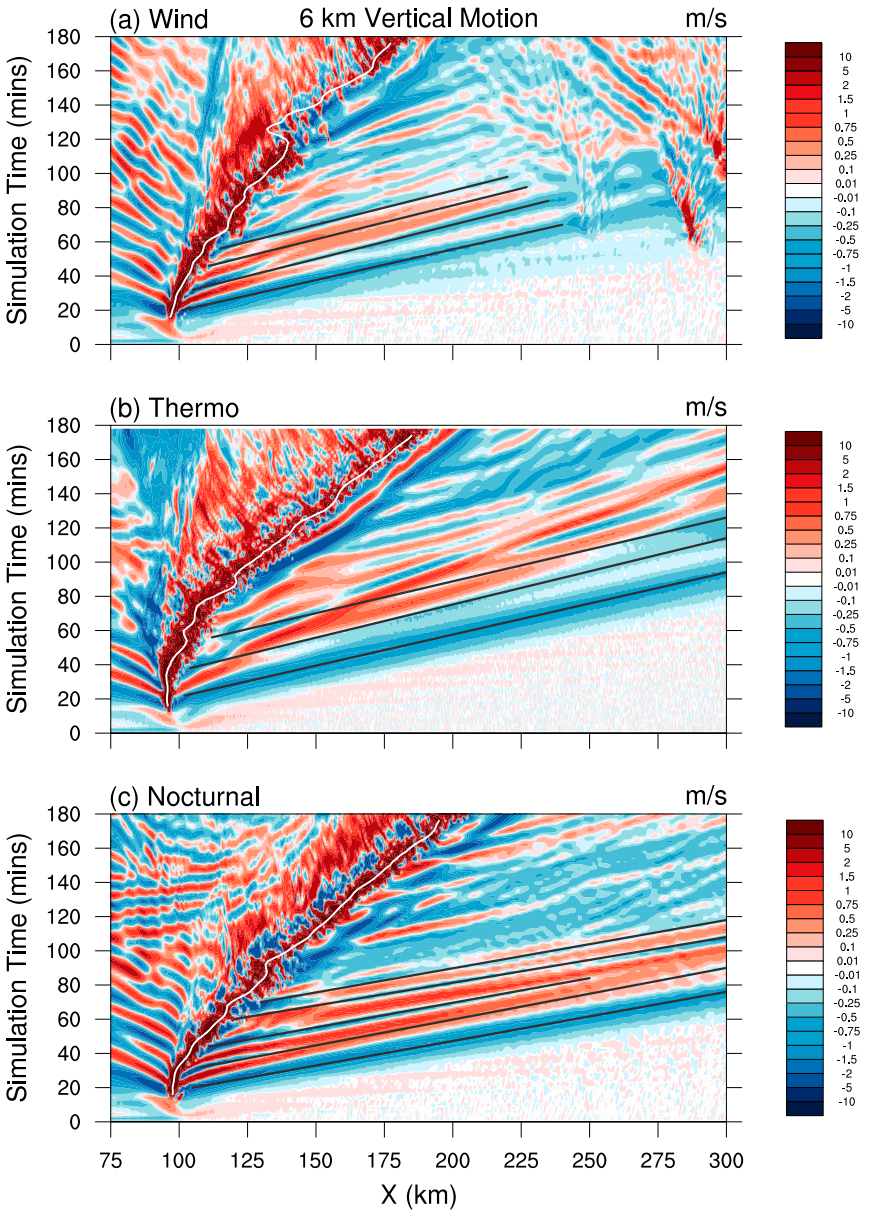

FIG. 16. As in Fig. 4, but for the (a) Wind, (b) Thermo, and (c) Nocturnal simulations and their respective $n = 1$ waves.

simulation, yet their vertical latent heating profiles differ greatly as the systems develop. The rates of latent heat release approach almost twice that of the Control simulation (cf. Figs. 9 and 15b), suggesting through theory that subsequent $n = 1$ waves should also be stronger. The gap in latent heating rates between 8 and 9 km for the first 40–50 min of the Thermo simulation is due to spurious clouds forming at that level throughout the domain that skew the 95th-percentile values of latent heating toward smaller rates.

Spectral analysis becomes increasingly useful in identifying $n = 1$ waves as the MCS and preconvective environment become more complex with the nocturnal thermodynamic initialization profile. The objective analysis is applied again to the 95th-percentile time series of updraft velocity, latent heat release, and descent ahead of the convection in the same manner as section 4a(1), and each have significant spectra around 0.20 cycles $(2\,\text{min})^{-1}$ as seen in Fig. 17b. Maximums in latent heat release rates can be subjectively identified with this kind of frequency in Fig. 15b, but the corresponding $n = 1$ gravity wave signature of deep tropospheric descent appears to be half as frequent in Fig. 16b. Results from the spectral analysis performed on this simulation indicate that there are likely more $n = 1$ gravity waves being generated and propagating ahead of the MCS than can be easily subjectively identified. The objective analysis also suggests that compared to the frequency of 0.12 cycles $(2\,\text{min})^{-1}$ for the Control and Wind simulations, this

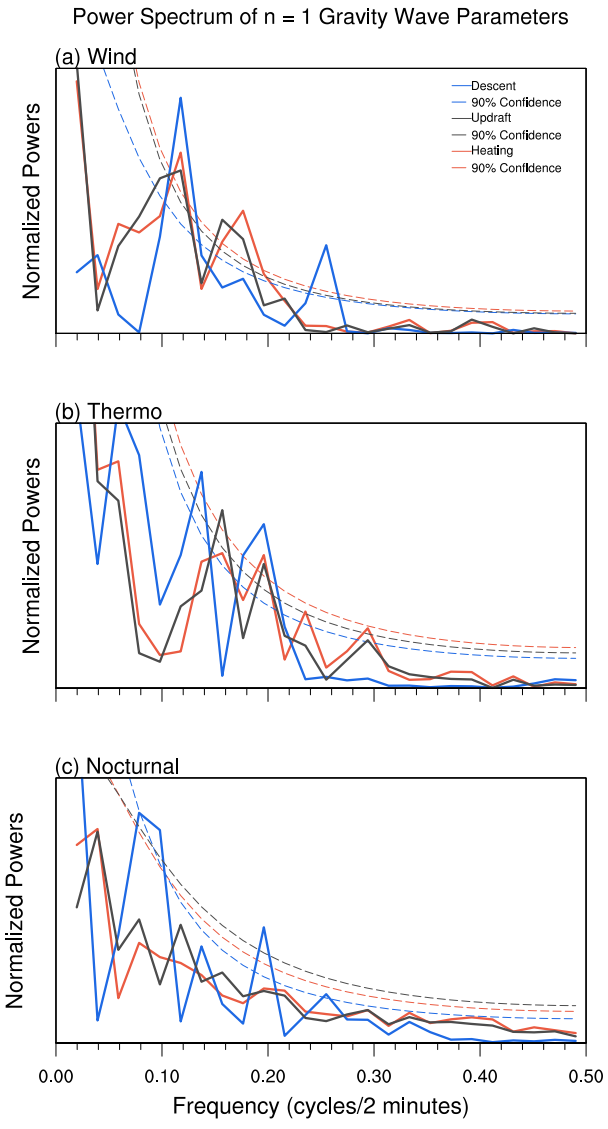

FIG. 17. As in Fig. 11, but for the (a) Wind, (b) Thermo, and (c) Nocturnal simulations.

nocturnal environment supports more frequent cellularity in the updrafts.

2) $n = 2$ GRAVITY WAVE GENERATION

The structure of latent cooling due to melting shows obvious similarities to the Control simulation (cf. Figs. 6 and 18b), where high rates of evaporation are present in the midlevels as opposed to the Wind simulation where the majority of evaporation occurs below cloud base. Many of the $n = 2$ gravity waves are generated in similar circumstances to the Control simulation as well. The first wave is generated just after the onset of precipitation to the surface, and as the storm begins to mature as evidenced by the development of a trailing stratiform region, another wave is generated around 40 min into the simulation as the horizontal extent of cooling expands. Twenty minutes later, rapidly increasing rates of latent cooling with contributions from both evaporation and melting are observed as a strong downdraft occurs within the storm, and the last subjectively identified wave of the simulation is generated shortly thereafter.

3) ENVIRONMENTAL RESPONSE

The first $n = 1$ wave of the simulation has almost double the magnitude of descent compared to the first $n = 1$ wave of the Control simulation due to the increased amounts of latent heat release within this MCS. While the first $n = 1$ wave acts to decrease the magnitude of MUCAPE by over 200 J kg^{-1} for the entire domain, shown by the first gray line in Fig. 20b, the second wave's influence is fleeting once it overruns the first $n = 2$ wave of the simulation as these wave types have opposing MUCAPE impacts. The second $n = 2$ wave has the greatest environmental influence as its associated ascent is the strongest and most expansive out of any of the $n = 2$ waves analyzed in the simulations thus far. This wave helps to increase the MUCAPE by 200 J kg^{-1}, counteracting the reduction by a previous $n = 1$ wave.

c. *Nocturnal environment*

The sounding used for this simulation, shown in Fig. 2d, incorporates the vertical wind profile of the Wind simulation and the thermodynamic profile of the Thermo simulation, emulating a nocturnal environment that features an LLJ and stable boundary layer. Despite the 20% relative humidity addition within the lowest 200 hPa, the MCS generated within this environment demonstrates a similar intensity and structure to the observed PECAN MCS from which the environment was sampled. Figure 23 shows a range–height indicator (RHI) scan taken from the S-band/Ka-band dual-polarization, dual-wavelength Doppler radar deployed during the field campaign [see Hubbert et al. (2018) for more details on the radar observations taken during PECAN]. At 0607 UTC 15 July 2015, the radar was located approximately 25 km to the southeast of the sampled MCS, offering an insight to the internal structure of the system. For comparison, a vertical cross section of radar reflectivity of the mature, simulated MCS is shown in Fig. 24. The similarity in intensity, structure, and horizontal expanse between the simulated and observed MCSs speaks to the validity of the initialization environment and dynamics within the idealized system.

As to be expected, the resulting MCS mimics aspects of those in the Wind and Thermo simulations. The extent of the stratiform region is modest compared to that of the Control and Thermo simulations as well as the actual observed MCS, a characteristic only shared with the Wind simulation (Fig. 3b). This indicates that vertical wind shear plays an important role in the development (or lack thereof) of the stratiform region, and subsequently also in the structure of latent cooling.

By every parameter, this is the strongest and longest sustained MCS out of all the simulations as it has both the higher MUCAPE of the Thermo simulation and the stronger line-normal shear of the Wind simulation (Rotunno et al. 1988; Markowski and Richardson 2011). This characteristic is blatantly apparent when comparing the updraft time series of the different simulations in Fig. 14. The rates of latent heating and

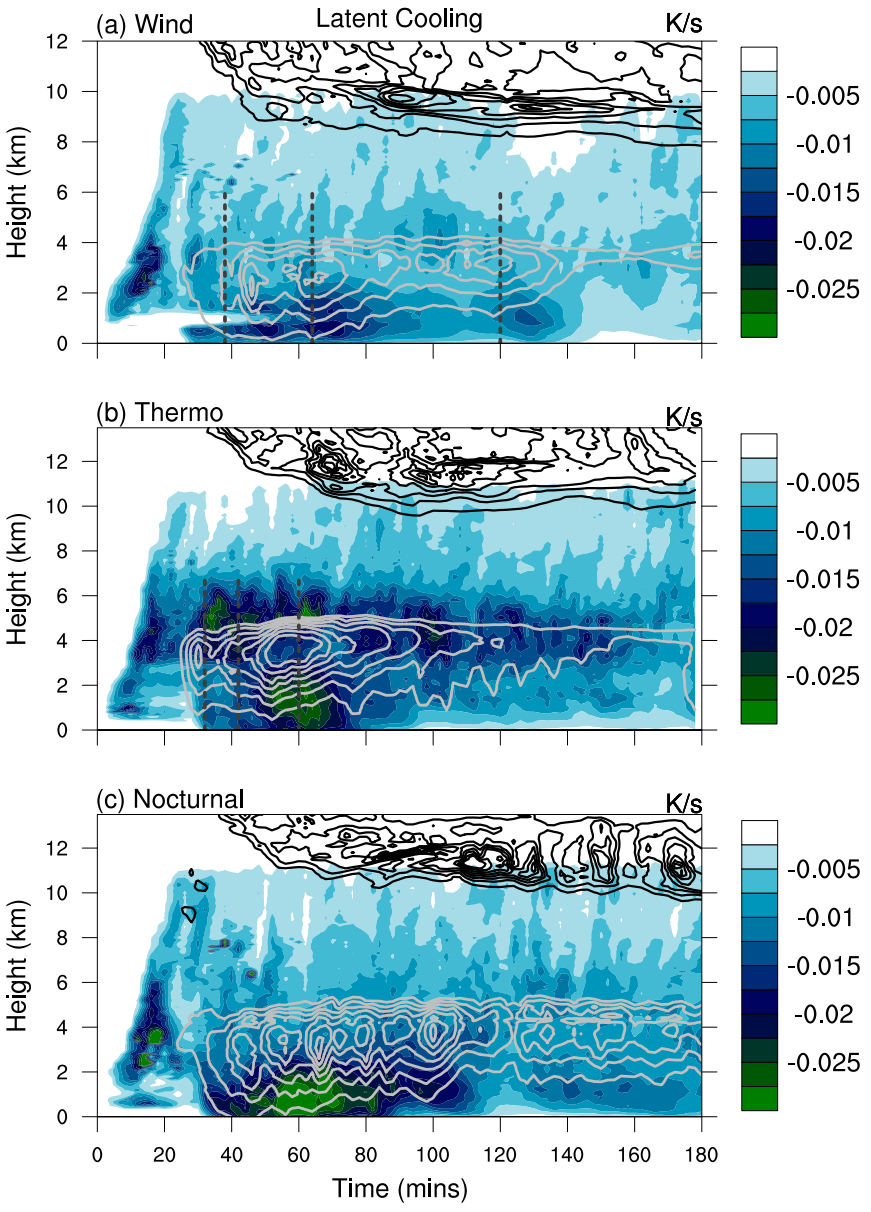

FIG. 18. As in Fig. 6, but for the (a) Wind, (b) Thermo, and (c) Nocturnal simulations and their respective $n = 2$ wave generation times as determined from Fig. 19. Note that the Nocturnal simulation does not have any analyzed $n = 2$ waves.

cooling, shown in Figs. 15c and 18c, respectively, are also the strongest, and thus so are the vertical motions associated with each wave mode (Figs. 16c and 19c).

1) GRAVITY WAVE GENERATION

Consistent with the other simulations, fluctuations in the intensity of the latent heat release govern the frequency and strength of the $n = 1$ waves. Spectral analysis of the $n = 1$ gravity wave parameters shown in Fig. 17c reveals a significant spectral peak of $n = 1$ gravity wave descent at a frequency of 0.20 cycles $(2\,\text{min})^{-1}$, the same frequency of descent as in the Thermo simulation. The activity within this MCS, however, conceals any signal of updraft cycling and latent heat fluctuations within the spectral analysis, rendering a direct comparison of $n = 1$ gravity wave generation to updraft cycling unfeasible.

Unique to this simulation is the presence of strong, easily identifiable periods of deep-tropospheric ascent immediately following the descent of the $n = 1$ waves. Previous studies have found that as the rates of microphysical heating subside temporarily during updraft cycling, a wave of upward motion throughout the depth of the troposphere propagates away from the MCS in response (e.g., Nicholls et al. 1991; McAnelly et al. 1997; Lane and Zhang 2011; Adams-Selin and Johnson 2013). While this process is true within all of the simulations, the

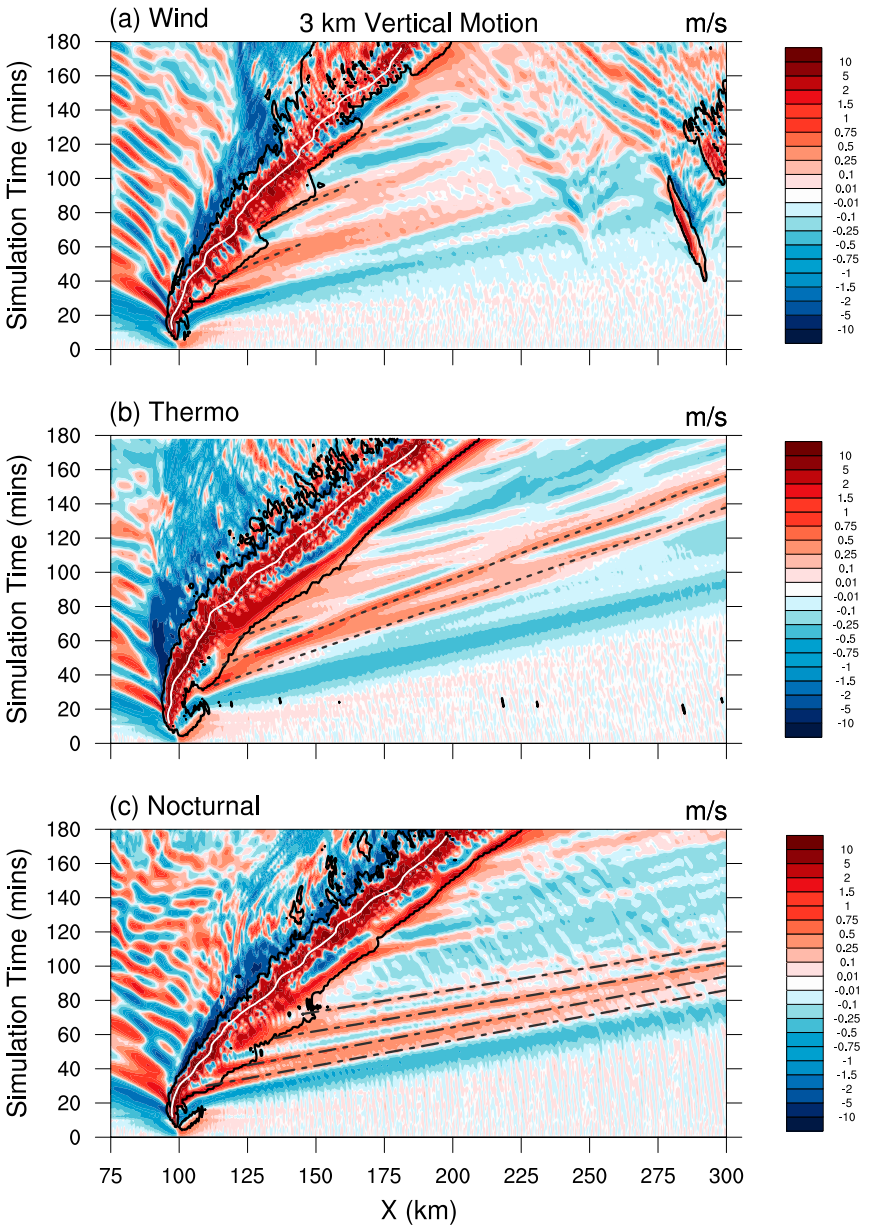

FIG. 19. As in Fig. 7, but for the $n = 2$ gravity waves in the (a) Wind and (b) Thermo simulations. (c) The broken lines show the positive vertical motion components of $n = 1$ gravity waves in the Nocturnal simulation. The black contours represent the 0.01 g kg^{-1} cloud mixing ratio.

response waves in this simulation are the only ones to have a notable impact on the environment.

The structure of latent cooling within this MCS mimics that of the Wind simulation, where the strongest evaporative cooling rates occur below cloud base as opposed to the Control and Thermo simulations in which much of the evaporative cooling occurs around the freezing level. Quite opposite from the Wind simulation, however, is the production and influence of $n = 2$ waves. From Fig. 19c, the periods of ascent at 3 km, denoted by the broken lines, are actually caused by the upward motion couplet of the $n = 1$ waves and are not associated with $n = 2$ waves. While $n = 2$ waves could be hidden among the motions of these couplets as well as other higher-order wave modes, this environment favors the strong deep-tropospheric ascent from the $n = 1$ wave couplets.

2) ENVIRONMENTAL RESPONSE

The descent associated with the $n = 1$ waves can be seen in Fig. 16c. As in the other simulations, the downward motion associated with these waves acts to dry and warm the column,

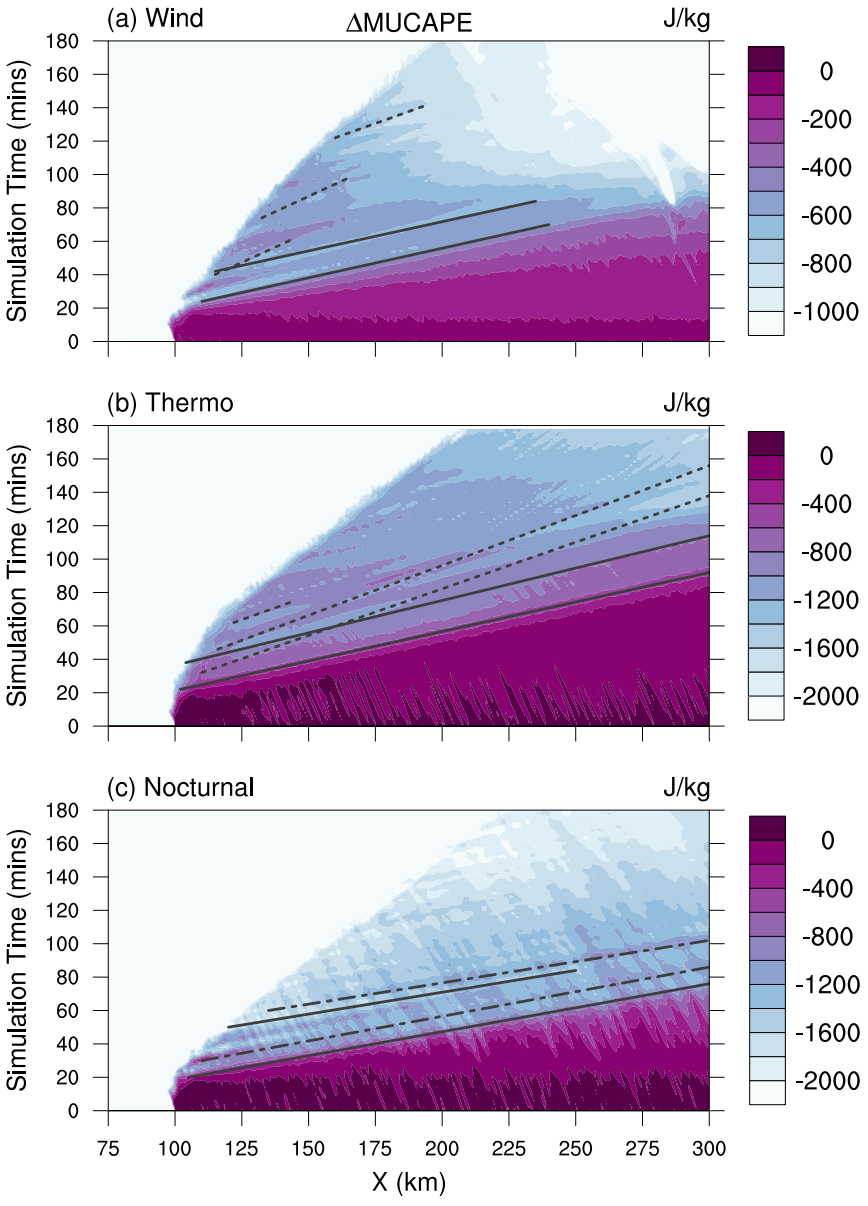

FIG. 20. As in Fig. 12, but for the $n = 1$ and 2 waves in the (a) Wind and (b) Thermo simulations. (c) Changes in CAPE from the updraft/downdraft couplets of $n = 1$ waves for the Nocturnal simulation, where the broken lines indicate upward motion from the $n = 1$ waves.

decreasing MUCAPE with each wave passage as shown in Fig. 20c. The ascent components of the $n = 1$ waves are substantial enough to be recognized in the lower levels as highlighted by the broken lines in Fig. 19c. There is the presence of a small stable layer overtopped by a trapping layer due to the curvature of the wind profile around 3 km, but the vertical motion associated with these features is most emphasized near 6 km, consistent with $n = 1$ low-frequency gravity waves rather than other processes. Similar to the $n = 2$ wave impacts in the Wind simulation, this ascent helps to destabilize the environment, aiding in new cloud development ahead of the convection with each wave passage (cf. Figs. 19a,c). As shown in Fig. 20c, the upward vertical motion associated with the $n = 1$ waves also aids in MUCAPE restoration as the accompanied drying and heating help to counteract the MUCAPE reduction from the descent portion of the $n = 1$ wave before it, as theorized in McAnelly et al. (1997). Su and Zhai (2017) observed similarly strong $n = 1$ wave couplets within their case study that eventually supported CI.

5. Discussion and conclusions

To extend the $n = 1$ gravity wave generation mechanism beyond theory, from fluctuations in the latent heating profile to

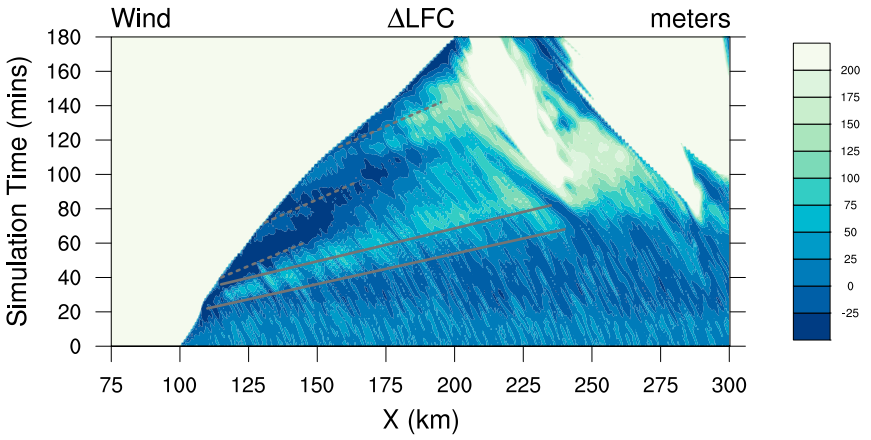

FIG. 21. As in Fig. 13, but for the Wind simulation and associated $n = 1$ and $n = 2$ waves.

updraft cyclicity, as well as to examine the potential of low-frequency gravity waves to support or suppress new and existing convection, four idealized cloud model simulations are conducted. These objectives are addressed within environments with complex vertical wind shear and nocturnal thermodynamic characteristics. Each simulation introduces considerable changes to the generated MCS that alter not only the internal dynamics of the system but also the way in which the low-frequency waves are generated and impact the environment.

These objectives are first tested within a highly idealized environment. Spectral analysis is performed on the 95th-percentile values of updraft velocity, latent heat release, and preconvective

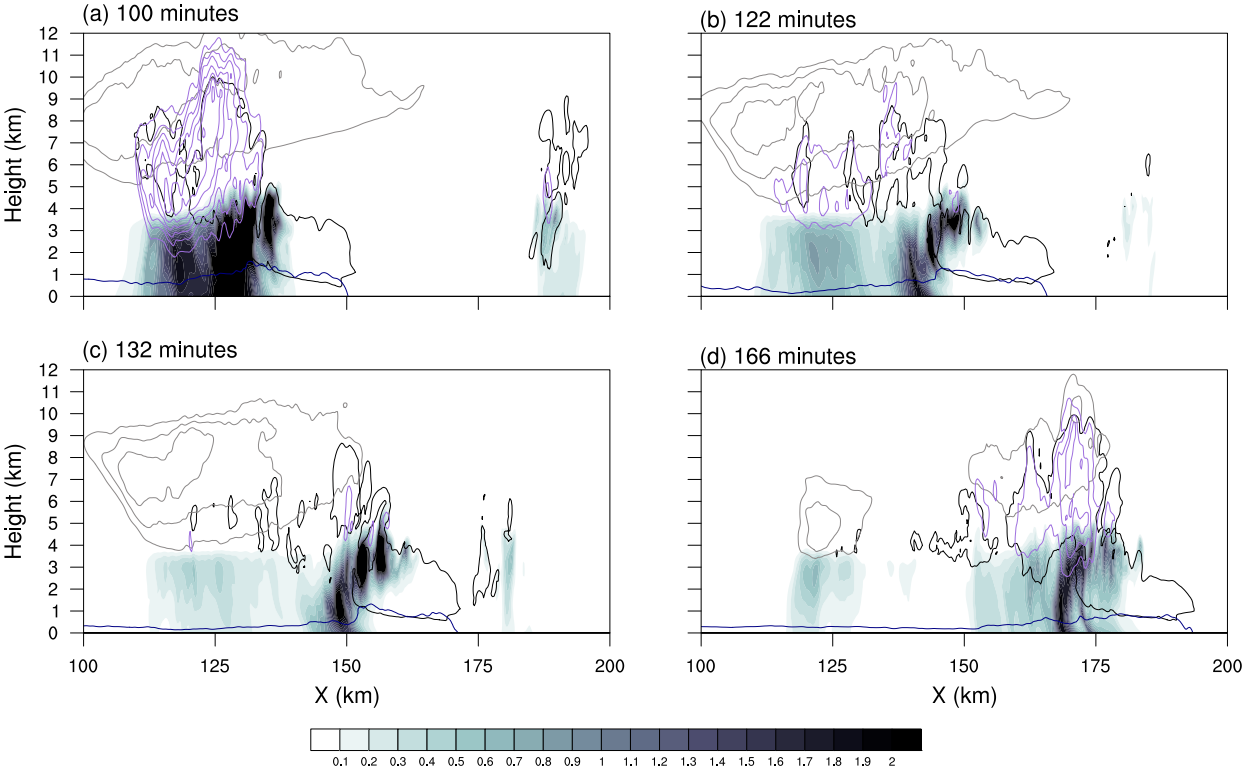

FIG. 22. Vertical cross sections of the hydrometeor composition of the MCS and downstream single convective cell at (a) 100, (b) 122, (c) 132, and (d) 166 min into the Wind simulation. The blue contour shows the location of the cold pool, the purple line contours represent q_g from 0.5 to 5 g kg^{-1} by 0.5 g kg^{-1}, the black contour is the q_c at 0.15 g kg^{-1}, the gray contours are q_i from 0 to 4 g kg^{-1} by 1 g kg^{-1}, and filled color contours show q_r (g kg^{-1}). Note: the y-axis domain was changed for this figure alone to a 10-km box centered about $y = 90$ km to capture the ingestion of the single cell.

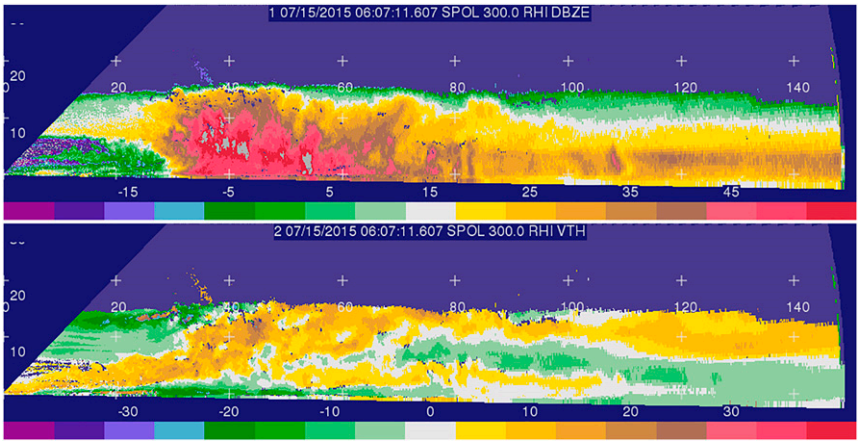

FIG. 23. An RHI scan of the observed PECAN MCS at 0607 UTC. (top) Radar reflectivity and (bottom) velocity, with respective magnitudes along the bottom of each panel. The numbers on the y and x axes of the panels delineate the height and distance in km from the radar, respectively.

descent and reveals that all three variables fluctuate at the same frequency of 0.12 cycles $(2\,\text{min})^{-1}$. These results strongly suggest that $n = 1$ waves and associated periods of deep-tropospheric descent over 100 km ahead of the MCS are generated periodically by variations within the latent heating profile due to the cellular nature of MCS updrafts.

What differs among the simulations regarding $n = 1$ waves is their general strength and frequency. Although the Wind simulation has slightly stronger updrafts and increased rates of latent heating compared to the Control simulation, they have identical frequencies for $n = 1$ gravity wave generation. The introduction of low-level, line-normal wind shear within this environment does not change the frequency of updraft redevelopment or low-frequency gravity wave generation, only the strength of the waves downstream due to enhanced latent heating within the system. The Thermo simulation, however, displays much more frequent redevelopment of the updrafts. Spectral analysis reveals matching spectra for the three $n = 1$ variables but at 0.20 cycles $(2\,\text{min})^{-1}$ compared to the 0.12 cycles $(2\,\text{min})^{-1}$ frequencies of the Control and Wind simulations. The introduction of the nocturnal environment, which is initialized with much greater MUCAPE compared to the Control and Wind simulations, acts to increase the frequency of updraft redevelopment, fluctuations in the latent heating profile, and $n = 1$ gravity wave generation. Regardless of their frequency, the $n = 1$ waves have a similar impact in all of the simulations in which the passage of each wave reduces MUCAPE and occasionally increases the LFC.

The generation mechanisms and environmental influence of the $n = 2$ gravity waves vary among the simulations considerably more than the $n = 1$ waves. Three waves are analyzed within the Control simulation which are generated in response to surges in latent cooling. The generation of the first $n = 2$ wave occurs as rain and hail first descend to the surface, and the second, stronger wave is generated when the horizontal expanse of latent cooling is increased due to the development of a trailing

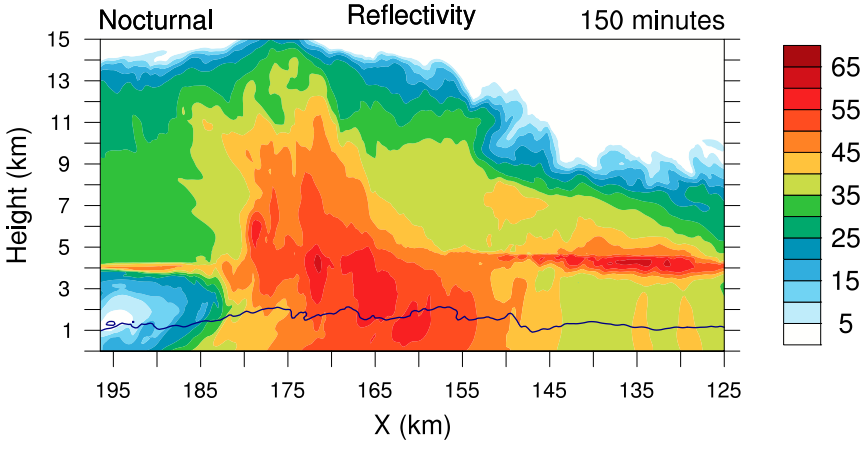

FIG. 24. Vertical cross section of reflectivity of the mature simulated MCS with the X axis reversed to match the orientation of the RHI scan in Fig. 23. The navy contour delineates the cold pool.

stratiform region. Although their thermodynamic profiles are vastly different, the Thermo and Control simulations share a very similar structure of latent cooling and $n = 2$ wave generation mechanisms. The rates of latent cooling are much stronger in the Thermo simulation, however, and therefore, so is the low-level ascent associated with the $n = 2$ waves ahead of the MCS. Within these simulations, there are strong rates of evaporative cooling at the melting level that only descend to the surface with increased hydrometeor fallout often seen within strong downdrafts. The Control and Thermo simulations share the same idealized vertical wind profile, implying that in environments with little upper-level wind shear atop more pronounced shear below, $n = 2$ gravity wave generation mechanisms are consistent among daytime and nocturnal MCSs.

The Control and Wind simulations share the same thermodynamic environment, yet the structure of latent cooling is vastly different. Evaporative cooling within the Control simulation is well distributed among the lower half of the troposphere, with the strongest rates of latent cooling occurring around the melting level. This simulation's lack of wind shear in the mid- to upper levels, in combination with weaker updraft velocities, prevents prolonged hail suspension, and with the first downdraft, both rain and hail descend to the surface and contribute to a strong latent cooling surge in the lower half of the troposphere. The Wind simulation, however, initially confines the majority of evaporative cooling to below cloud base. The deeper wind shear and stronger updrafts act to suspend hail within the convection for longer, and consequently the first onset of precipitation to the surface lacks latent cooling due to melting hydrometeors and therefore lacks the latent cooling response needed to initiate an $n = 2$ wave at this time. This dependency is witnessed in all of the simulations: $n = 2$ waves are only generated among surges of both melting and evaporation.

The Nocturnal simulation is an outlier to the rest in many ways. Numerous studies have detailed how $n = 1$ waves can have both deep-tropospheric descent and ascent components (e.g., Nicholls et al. 1991; McAnelly et al. 1997; Su and Zhai 2017). The descent component is generated in response to increases in latent heat release as thoroughly demonstrated in this study; however, when the latent heating subsides during updraft regeneration, the environment becomes more favorable for the generation of the ascent portion of the $n = 1$ wave. These periods of ascent are present in the other simulations but are dwarfed by other wave motions; however, in this environment, the updraft couplets are the most impactful feature in the simulation.

The upward vertical motion associated with the low-frequency gravity waves in these simulations proves advantageous in many ways. The ascent from an $n = 2$ wave in the Wind simulation revives a decaying single cell ahead of the convective line, guaranteeing its sustainment and propagation until it is overtaken by the parent system. The extra buoyancy and moisture from this cell in turn revives the MCS, a process that would not have occurred without the initial support from the $n = 2$ wave. The ascent from the $n = 2$ waves in this simulation also acts to create a moist layer ahead of the MCS, and as the waves propagate away from the system, the clouds are drawn out with them into the favorable environment. A similar cloud development process is observed in the Nocturnal simulation due to the ascent of the $n = 1$ waves, extending the possibility of discrete propagation to any low-frequency gravity wave that can provide enough lift.

A particular challenge unique to nocturnal MCSs is the ability to lift parcels to their LFC when inhibited by a stable boundary layer and lack of surface-based CAPE. Low-level outflow structures in nocturnal MCSs range from traditional cold pools to gravity waves (e.g., Parker 2008; Schumacher 2009; Parker 2021), and previous studies have examined how bores and solitary waves may play an important role in this lifting process (e.g., Koch et al. 1991; Knupp 2006; Coleman and Knupp 2011; Parsons et al. 2019), including numerous studies from the PECAN field campaign (e.g., Geerts et al. 2017; Grasmick et al. 2018; Wilson et al. 2018; Haghi et al. 2019; Zhang et al. 2020). The present study demonstrates the potential for low-frequency gravity waves to act as a similar kind of catalyst.

Acknowledgments. This research was supported by the National Science Foundation Grants AGS-1636663 and AGS-1636667. High-performance computing support from Cheyenne (https://doi.org/10.5065/D6RX99HX) was provided by NCAR's Computational and Information Systems Laboratory, sponsored by the National Science Foundation. The authors also thank Dr. Elizabeth Barnes for her guidance on statistical analysis used in this research, and the five anonymous reviewers for their helpful contributions.

REFERENCES

Adams-Selin, R. D., 2020a: Impact of convectively generated low-frequency gravity waves on evolution of mesoscale convective systems. *J. Atmos. Sci.*, **77**, 3441–3460, https://doi.org/10.1175/JAS-D-19-0250.1.

——, 2020b: Sensitivity of MCS low-frequency gravity waves to microphysical variations. *J. Atmos. Sci.*, **77**, 3461–3477, https://doi.org/10.1175/JAS-D-19-0347.1.

——, and R. H. Johnson, 2013: Examination of gravity waves associated with the 13 March 2003 bow echo. *Mon. Wea. Rev.*, **141**, 3735–3756, https://doi.org/10.1175/MWR-D-12-00343.1.

Bryan, G. H., and H. Morrison, 2012: Sensitivity of a simulated squall line to horizontal resolution and parameterization of microphysics. *Mon. Wea. Rev.*, **140**, 202–225, https://doi.org/10.1175/MWR-D-11-00046.1.

——, R. Rotunno, and J. M. Fritsch, 2007: Roll circulations in the convective region of a simulated squall line. *J. Atmos. Sci.*, **64**, 1249–1266, https://doi.org/10.1175/JAS3899.1.

Coleman, T. A., and K. R. Knupp, 2011: Radiometer and profiler analysis of the effects of a bore and a solitary wave on the stability of the nocturnal boundary layer. *Mon. Wea. Rev.*, **139**, 211–223, https://doi.org/10.1175/2010MWR3376.1.

Fovell, R. G., 2002: Upstream influence of numerically simulated squall-line storms. *Quart. J. Roy. Meteor. Soc.*, **128**, 893–912, https://doi.org/10.1256/0035900021643737.

——, G. L. Mullendore, and S.-H. Kim, 2006: Discrete propagation in numerically simulated nocturnal squall lines. *Mon. Wea. Rev.*, **134**, 3735–3752, https://doi.org/10.1175/MWR3268.1.

Fritsch, J., and G. Forbes, 2001: Mesoscale convective systems. *Severe Convective Storms*, Springer, 323–357.

——, R. Kane, and C. Chelius, 1986: The contribution of mesoscale convective weather systems to the warm-season precipitation in the United States. *J. Appl. Meteor. Climatol.*, **25**, 1333–1345, https://doi.org/10.1175/1520-0450(1986)025<1333:TCOMCW>2.0.CO;2.

Gallus, W. A., and R. H. Johnson, 1991: Heat and moisture budgets of an intense midlatitude squall line. *J. Atmos. Sci.*, **48**, 122–146, https://doi.org/10.1175/1520-0469(1991)048<0122:HAMBOA>2.0.CO;2.

Geerts, B., and Coauthors, 2017: The 2015 Plains Elevated Convection at Night field project. *Bull. Amer. Meteor. Soc.*, **98**, 767–786, https://doi.org/10.1175/BAMS-D-15-00257.1.

Grasmick, C., B. Geerts, D. D. Turner, Z. Wang, and T. Weckwerth, 2018: The relation between nocturnal MCS evolution and its outflow boundaries in the stable boundary layer: An observational study of the 15 July 2015 MCS in PECAN. *Mon. Wea. Rev.*, **146**, 3203–3226, https://doi.org/10.1175/MWR-D-18-0169.1.

Haghi, K. R., and Coauthors, 2019: Bore-ing into nocturnal convection. *Bull. Amer. Meteor. Soc.*, **100**, 1103–1121, https://doi.org/10.1175/BAMS-D-17-0250.1.

Hitchcock, S. M., R. S. Schumacher, G. R. Herman, M. C. Coniglio, M. D. Parker, and C. L. Ziegler, 2019: Evolution of pre-and postconvective environmental profiles from mesoscale convective systems during PECAN. *Mon. Wea. Rev.*, **147**, 2329–2354, https://doi.org/10.1175/MWR-D-18-0231.1.

Houze, R. A., Jr., 2004: Mesoscale convective systems. *Rev. Geophys.*, **42**, RG4003, https://doi.org/10.1029/2004RG000150.

Hubbert, J. C., J. W. Wilson, T. M. Weckwerth, S. M. Ellis, M. Dixon, and E. Loew, 2018: S-Pol's polarimetric data reveal detailed storm features (and insect behavior). *Bull. Amer. Meteor. Soc.*, **99**, 2045–2060, https://doi.org/10.1175/BAMS-D-17-0317.1.

Knupp, K., 2006: Observational analysis of a gust front to bore to solitary wave transition within an evolving nocturnal boundary layer. *J. Atmos. Sci.*, **63**, 2016–2035, https://doi.org/10.1175/JAS3731.1.

Koch, S. E., P. B. Dorian, R. Ferrare, S. Melfi, W. C. Skillman, and D. Whiteman, 1991: Structure of an internal bore and dissipating gravity current as revealed by Raman lidar. *Mon. Wea. Rev.*, **119**, 857–887, https://doi.org/10.1175/1520-0493(1991)119<0857:SOAIBA>2.0.CO;2.

Lane, T. P., and M. J. Reeder, 2001: Convectively generated gravity waves and their effect on the cloud environment. *J. Atmos. Sci.*, **58**, 2427–2440, https://doi.org/10.1175/1520-0469(2001)058<2427:CGGWAT>2.0.CO;2.

——, and F. Zhang, 2011: Coupling between gravity waves and tropical convection at mesoscales. *J. Atmos. Sci.*, **68**, 2582–2598, https://doi.org/10.1175/2011JAS3577.1.

Mapes, B. E., 1993: Gregarious tropical convection. *J. Atmos. Sci.*, **50**, 2026–2037, https://doi.org/10.1175/1520-0469(1993)050<2026:GTC>2.0.CO;2.

Markowski, P., and Y. Richardson, 2011: *Mesoscale Meteorology in Midlatitudes*. Vol. 2. John Wiley and Sons, 253–258.

McAnelly, R. L., J. E. Nachamkin, W. R. Cotton, and M. E. Nicholls, 1997: Upscale evolution of MCSs: Doppler radar analysis and analytical investigation. *Mon. Wea. Rev.*, **125**, 1083–1110, https://doi.org/10.1175/1520-0493(1997)125<1083:UEOMDR>2.0.CO;2.

Morrison, H., G. Thompson, and V. Tatarskii, 2009: Impact of cloud microphysics on the development of trailing stratiform precipitation in a simulated squall line: Comparison of one- and two-moment schemes. *Mon. Wea. Rev.*, **137**, 991–1007, https://doi.org/10.1175/2008MWR2556.1.

Naylor, J., and M. S. Gilmore, 2012: Convective initiation in an idealized cloud model using an updraft nudging technique. *Mon. Wea. Rev.*, **140**, 3699–3705, https://doi.org/10.1175/MWR-D-12-00163.1.

Nicholls, M. E., R. A. Pielke, and W. R. Cotton, 1991: Thermally forced gravity waves in an atmosphere at rest. *J. Atmos. Sci.*, **48**, 1869–1884, https://doi.org/10.1175/1520-0469(1991)048<1869:TFGWIA>2.0.CO;2.

Parker, M. D., 2008: Response of simulated squall lines to low-level cooling. *J. Atmos. Sci.*, **65**, 1323–1341, https://doi.org/10.1175/2007JAS2507.1.

——, 2021: Self-organization and maintenance of simulated nocturnal convective systems from PECAN. *Mon. Wea. Rev.*, **149**, 999–1022, https://doi.org/10.1175/MWR-D-20-0263.1.

——, and R. H. Johnson, 2004: Structures and dynamics of quasi-2D mesoscale convective systems. *J. Atmos. Sci.*, **61**, 545–567, https://doi.org/10.1175/1520-0469(2004)061<0545:SADOQM>2.0.CO;2.

Parsons, D. B., K. R. Haghi, K. T. Halbert, B. Elmer, and J. Wang, 2019: The potential role of atmospheric bores and gravity waves in the initiation and maintenance of nocturnal convection over the Southern Great Plains. *J. Atmos. Sci.*, **76**, 43–68, https://doi.org/10.1175/JAS-D-17-0172.1.

Peters, J. M., and R. S. Schumacher, 2016: Dynamics governing a simulated mesoscale convective system with a training convective line. *J. Atmos. Sci.*, **73**, 2643–2664, https://doi.org/10.1175/JAS-D-15-0199.1.

Rotunno, R., J. B. Klemp, and M. L. Weisman, 1988: A theory for strong, long-lived squall lines. *J. Atmos. Sci.*, **45**, 463–485, https://doi.org/10.1175/1520-0469(1988)045<0463:ATFSLL>2.0.CO;2.

Schmidt, J. M., and W. R. Cotton, 1990: Interactions between upper and lower tropospheric gravity waves on squall line structure and maintenance. *J. Atmos. Sci.*, **47**, 1205–1222, https://doi.org/10.1175/1520-0469(1990)047<1205:IBUALT>2.0.CO;2.

Schumacher, R. S., 2009: Mechanisms for quasi-stationary behavior in simulated heavy-rain-producing convective systems. *J. Atmos. Sci.*, **66**, 1543–1568, https://doi.org/10.1175/2008JAS2856.1.

——, and R. H. Johnson, 2005: Organization and environmental properties of extreme-rain-producing mesoscale convective systems. *Mon. Wea. Rev.*, **133**, 961–976, https://doi.org/10.1175/MWR2899.1.

Skamarock, W. C., 2004: Evaluating mesoscale NWP models using kinetic energy spectra. *Mon. Wea. Rev.*, **132**, 3019–3032, https://doi.org/10.1175/MWR2830.1.

Su, T., and G. Zhai, 2017: The role of convectively generated gravity waves on convective initiation: A case study. *Mon. Wea. Rev.*, **145**, 335–359, https://doi.org/10.1175/MWR-D-16-0196.1.

Trapp, R. J., and J. M. Woznicki, 2017: Convectively induced stabilizations and subsequent recovery with supercell thunderstorms during the Mesoscale Predictability Experiment (MPEX). *Mon. Wea. Rev.*, **145**, 1739–1754, https://doi.org/10.1175/MWR-D-16-0266.1.

Weisman, M. L., and J. B. Klemp, 1982: The dependence of numerically simulated convective storms on vertical wind shear and buoyancy. *Mon. Wea. Rev.*, **110**, 504–520, https://doi.org/10.1175/1520-0493(1982)110<0504:TDONSC>2.0.CO;2.

——, W. C. Skamarock, and J. B. Klemp, 1997: The resolution dependence of explicitly modeled convective systems. *Mon. Wea. Rev.*, **125**, 527–548, https://doi.org/10.1175/1520-0493(1997)125<0527:TRDOEM>2.0.CO;2.

Wilks, D. S., 2011: *Statistical Methods in the Atmospheric Sciences*. Academic Press, 676 pp.

Wilson, J., S. Trier, D. Reif, R. Roberts, and T. Weckwerth, 2018: Nocturnal elevated convection initiation of the PECAN 4 July hailstorm. *Mon. Wea. Rev.*, **146**, 243–262, https://doi.org/10.1175/MWR-D-17-0176.1.

Zhang, S., D. B. Parsons, and Y. Wang, 2020: Wave disturbances and their role in the maintenance, structure, and evolution of a mesoscale convection system. *J. Atmos. Sci.*, **77**, 51–77, https://doi.org/10.1175/JAS-D-18-0348.1.